Journal of Materials Chemistry A

PAPER

View Article Online
View Journal | View Issue

Cite this: J. Mater. Chem. A, 2016, 4, 11672

High-density platinum nanoparticle-decorated titanium dioxide nanofiber networks for efficient capillary photocatalytic hydrogen generation†

Zhaodong Li,[a] Chunhua Yao,[a] Yi-Cheng Wang,[b] Solomon Mikael,[c] Sundaram Gunasekaran,[b] Zhenqiang Ma,[c] Zhiyong Cai*[d] and Xudong Wang*[a]

Received 9th June 2016
Accepted 1st July 2016

DOI: 10.1039/c6ta04846c

www.rsc.org/MaterialsA

Aldehyde-functionalized cellulose nanofibers (CNFs) were applied to synthesize Pt nanoparticles (NPs) on CNF surfaces *via* on-site Pt ion reduction and achieve high concentration and uniform Pt NP loading. ALD could then selectively deposit TiO_2 on CNFs and keep the Pt NPs uncovered due to their drastically different hydro-affinity properties. The high-temperature ALD process also simultaneously improved the crystallinity of Pt NPs and decomposed the CNF template leaving a pure anatase phase TiO_2 nanofiber network decorated with high-density Pt NPs (up to 11.05 wt%). The as-prepared fibrous Pt–TiO_2 network photocatalyst was integrated with CNF strips to develop a capillary setup for photocatalyzed hydrogen generation. Better reaction kinetics and higher efficiency were achieved from the capillary design compared to conventional in-electrolyte reactions. The initial H_2 generation rates were 100.56–138.69 mmol g^{-1} h^{-1} from the capillary setup based on different Pt NP loadings, which were 123.3–288.6% larger than those of the in-electrolyte setup (25.88–62.11 mmol g^{-1} h^{-1}). This 3D nanofibrous Pt–TiO_2 capillary photocatalyst offers a brand new solution for improving the throughput of photocatalytic hydrogen production.

Introduction

Hydrogen (H_2) fuel is a very promising green and sustainable energy source with high energy capacity and zero emission.[1] However, ~95% of the current H_2 supply in the world depends on reforming fossil fuels, which is unsustainable and generates greenhouse gases such as CO_2 in the atmosphere.[2] Therefore, producing H_2 from renewable sources holds great promise to solve the energy crisis and tackle the global warming issue.[3] Led by the pioneering discovery of H_2 evolution through the photocatalytic water splitting phenomenon on a titanium dioxide (TiO_2) electrode in the early 1970s,[4,5] plenty of explorations have been performed on various semiconductor catalysts to produce H_2 utilizing solar energy.[3,6–8] Integrating platinum (Pt) with TiO_2 surfaces has been found to be a very promising catalyst combination strategy for photocatalyzed redox reactions owing to their high stability for a long time and large Schottky barrier efficient electron–hole separation.[9,10] Sacrificial reagents are typically introduced as electron donors/acceptors to improve the photocatalytic reaction efficiency.[11–13] Although more Pt is believed to be beneficial for tolerating more photoexcited electrons to facilitate photocatalytic reactions,[14] the optimal amount of Pt loading on photocatalysts, either by photodeposition[15–17] or chemical reduction,[14,18] was usually below ~5 wt%. It is believed that excess Pt could compete for the photocatalytic sites on TiO_2 surfaces for sacrificial reagent adsorption resulting in low H_2 throughput.[14,19] Besides, other valence states of Pt, such as platinum oxide (PtO) or platinum dioxide (PtO_2), also might co-exist with elemental Pt due to pH variation in Pt impregnation processes, which jeopardizes the catalytic capability of metallic Pt.[15,20]

In addition, the nanostructure morphology is another important factor that can drastically impact the performance of photocatalysis. Among different nanoscale structures, three-dimensional (3D) mesoporous structures, such as branched nanowire architecture and nanofiber networks, are considered as promising configurations for photocatalyst fabrication.[3,21–23] They could provide an ultrahigh surface area for a large amount of metal nanoparticle (NP) loading and excellent structural continuity for rapid charge transport. They could also improve the light harvesting efficiency due to enhanced light scattering effects. Natural cellulose-based

[a]Department of Materials Science and Engineering, University of Wisconsin-Madison, Madison, WI 53706, USA. E-mail: xudong.wang@wisc.edu

[b]Department of Biological Systems Engineering, University of Wisconsin-Madison, Madison, WI 53706, USA

[c]Department of Electrical and Computer Engineering, University of Wisconsin-Madison, Madison, WI 53706, USA

[d]Forest Products Laboratory, USDA Forest Service, Madison, WI 53726, USA. E-mail: zcai@fs.fed.us

† Electronic supplementary information (ESI) available: Experimental details and analysis results such as SEM images, XPS, EDS, and XRD. Experimental apparatus, RGA calibration data, and H_2 yield of the as-prepared samples. See DOI: 10.1039/c6ta04846c

nanomaterials such as cellulose nanofibers (CNFs) are one of the widely used large-scale renewable 3D mesoporous structures owing to their great abundance, low cost, bio-compatibility and degradability.[24,25] They have been successfully utilized as remarkable templates for fabricating functional 3D nanostructures with extremely large porosity. Recently, based on the 3D CNF-templated TiO_2 nanostructures and taking advantage of the excellent hydrophilic properties of CNFs, we developed a novel high-performance capillary photoelectrochemical (PEC) photoanode that could perform PEC water oxidation in air with enhanced reaction kinetics.[24] However, in this PEC system, H_2 production was still in the electrolyte and on the surface of the counter electrode. To fully utilize the advantage of the capillary system, both reduction and oxidation (redox) reactions should be implemented in the capillary fashion. This requires the development of a full photocatalytic redox system with the 3D mesoporous hydrophilic configuration. Noting that the repeating units with reactive groups on cellulose are readily functionalized,[26] we hypothesized that reductive ligands could be created on cellulose surfaces and used to produce Pt on-site.

In this paper, CNFs were functionalized with aldehyde groups, which were successfully used to reduce Pt ions and form Pt NPs. High density Pt NPs were created on CNF networks. Atomic layer deposition (ALD) of TiO_2 completely converted the CNF template into anatase TiO_2 fibers without affecting the Pt NP loading. This 3D fibrous Pt–TiO_2 network structure was used as the photocatalyst in a capillary hydrogen generation system and a substantially higher H_2 generation rate was achieved compared to the conventional in-electrolyte setup. This research demonstrated a new solution to the efficient production of H_2 fuel from solar energy.

Experimental section

Synthesis of Pt NP-decorated CNFs

The main material used in this project is cellulose nanofibers (CNFs) isolated through a combination of TEMPO treatment and homogenization processing. The CNF hydrogel was oxidized in 0.05 M $NaIO_4$ solution to generate aldehyde functional groups. The dialdehyde-functionalized CNF hydrogel was then immersed in 0.01 M chloroplatinic acid (H_2PtCl_6) solution at 80 °C for 13 hours. The on-site reduction of Pt ions yielded high density Pt NPs on CNF surfaces. After gently rinsing the obtained Pt NP decorated CNF hydrogel in deionized (DI) water several times, the hydrogel was then frozen by using liquid nitrogen in an ethanol bath. Then, the frozen hydrogel was immediately and quickly transferred into the vacuum chamber of a Labconco 4.5 Liter Free Zone Freeze Dry System (Labconco, MO, USA) at a stable pressure of ~35 mTorr for 12 hours at room temperature, where sublimation of the ice yielded a nanofibrous structure cellulose film with Pt NPs on the surface. In order to obtain different Pt NP loadings, three processing times, 144, 180, and 200 hours, were selected to oxidize the CNF hydrogel, which were then used to produce Pt NPs within the same time frame and marked as C1, C2, and C3, respectively.

ALD of TiO_2 conversion

The Pt-CNF template was loaded into the ALD reaction chamber for 20 cycles of TiO_2 overcoating at 150 °C and subsequent 150 cycles of TiO_2 growth at 300 °C, which yielded the thickness of polycrystalline TiO_2 to be ~17 nm. The ALD growth cycle consisted of 0.5 s H_2O pulsing + 60 s N_2 purging + 0.5 s titanium tetrachloride ($TiCl_4$) pulsing + 60 s N_2 purging. The 150 °C ALD deposition process introduced a thin TiO_2 layer (~2 nm) to replicate the fibrous structure of Pt-CNFs, and the following high temperature ALD process at 300 °C made a continuous coverage of anatase TiO_2 as well as completely decomposed the CNFs leaving the fibrous nanotubular TiO_2 with preserved Pt nanoparticles on its surface.

Sample characterization

The morphologies of the as-prepared Pt-CNF template and Pt–TiO_2 photocatalyst were characterized by LEO 1530 GEMINI scanning electron microscopy (Zeiss, Germany). X-ray photoelectron spectroscopy (XPS) measurements were conducted for the elemental analysis on a Thermo Scientific K-alpha XPS system with an Al Kα source. Tecnai TF-30 transmission electron microscopy (FEI, OR, USA) and X-ray diffraction (Bruker D8, Bruker, MA, USA) were used to study the crystal structure of the Pt NPs formed on the CNF surface and the corresponding Pt–TiO_2 heterostructures. To quantify the final Pt loading as a function of the CNF oxidation time, ICP spectrometry (Optima 2000 ICP-AES, PerkinElmer, MA, USA) and EDS were performed on three Pt–TiO_2 samples (T1, T2 and T3). In the ICP measurements, a certain amount of each Pt–TiO_2 sample was weighted and put into a beaker with the subsequent addition of 15 mL aqua regia solution ($HCl : HNO_3 = 3 : 1$). The beaker was then heated to 70 °C and vigorously stirred for 3 hours to dissolve all Pt in the sample. The solution was thereafter filtered and DI water was added to the filtrate to fix the volume at 112 mL. Besides, the ICP Pt standard solution (1000 mg L^{-1}, Sigma-Aldrich, MO, USA) was diluted for reference solutions with three different concentrations (0.1 mg L^{-1}, 1.0 mg L^{-1}, and 10.0 mg L^{-1}). Finally, these three reference solutions and the filtered solution of each Pt–TiO_2 sample were injected into the ICP system to characterize the Pt concentrations. The S_{BET} of the Pt–TiO_2 photocatalyst was analyzed by nitrogen adsorption using Quantachrome Autosorb-1 equipment (Quantachrome Instruments, FL, USA). Prior to nitrogen adsorption measurements, each sample was transferred into a glass tube and degassed at 120 °C for 12 hours.

Setup for hydrogen production *via* photocatalytic reaction

For the capillary photocatalysis setup, the as-synthesized fibrous Pt–TiO_2 network structure was integrated with an untreated CNF stripe by the following procedures: first, the CNF block was carved into a chair-like shape. Then, 0.0157 g Pt–TiO_2 photocatalyst was settled on this CNF "chair" and fixed by using large mesh cheesecloth. The integrated CNF-based photocatalytic system was then hung in a quartz flask, and thereafter the whole apparatus was well sealed with one port opened in the

water for further H_2 collection. The other port of the flask was connected to the upper flask through a glass valve, where appropriate amounts of pure DI water and sacrificial reactant methanol were filled ($H_2O : CH_3OH = 4 : 1$ in volume) (Fig. S1a†). Before the illumination, Ar gas with a flow rate of 70 sccm was introduced into the methanol solution for deaeration and system purging for one hour. Then the glass valve in the upper flask (red circle in top left picture of Fig. S1b†) was opened to allow a suitable amount of methanol aqueous solution to flow into the bottom quartz flask, where the bottom portion of the CNF block was in touch with the electrolyte while the Pt–TiO_2 photoactive portion was exposed in the space. Instead, the whole Pt–TiO_2 photocatalyst was immersed into the electrolyte for the conventional in-electrolyte reaction (Fig. S2†). Light illumination was provided by a 150 W xenon arc lamp (Newport Corporation, Irvine, CA), and the intensity at the Pt–TiO_2 photocatalyst position was adjusted to be 70 mW cm^{-2} to restrict the rise of the system temperature by the light irradiation. The backside of the flask was flushed with cold water during the photoreaction process. The evolved gas was collected in a graduated flask and the H_2 amount was characterized with a Spectra Products Residual Gas Analysis (RGA) mass spectrometry system (MKS Instruments, Wilmington, MA, USA). In order to determine the amount of H_2 (mL), standard H_2 (Industrial Grade, Airgas, PA, USA) in certain volumes was also utilized for calibration. The peak areas of the signal were calculated at a constant total pressure of 2.53×10^{-5} Torr (Fig. S3†). By comparing the signal peak areas to the calibration data, the volume of the H_2 in the collected gas sample can be obtained. Several molar mass channels were simultaneously used to detect the possible components of the collected gas sample (Fig. S4 and Table S1†).

Results and discussion

The CNF hydrogel was employed as the starting material to produce a high-density Pt nanoparticle-decorated TiO_2 nanofiber network (Scheme 1). The CNF hydrogel was first immersed into $NaIO_4$ solution for aldehyde functionalization. Under desired conditions (see details in the Experimental section), the two OH groups on the repeating unit of cellulose were oxidized to aldehyde groups. Second, the on-site reduction of Pt ions by aldehyde groups yielded high density Pt NPs on CNF surfaces when the dialdehyde-functionalized CNF hydrogel was placed in chloroplatinic acid (H_2PtCl_6) solution. Finally, the obtained Pt NP-decorated CNF hydrogel was freeze dried to form a mesoporous structure. Subsequent ALD of TiO_2 converted CNFs to tubular TiO_2 nanofibers with Pt NPs exposed on the surfaces.

The as-prepared high-density Pt NP-decorated CNF network (Pt-CNF) was first observed by scanning electron microscopy (SEM). As shown in Fig. 1a, Pt NPs appeared in clusters of several (~2–6) individuals agglomerated together, which were evenly distributed over the entire CNF network. Meanwhile, the high-porosity network structure of the CNF was nearly unchanged after a long-time on-site Pt ion reduction reaction and the average fiber diameter remained at ~15 nm (inset of Fig. 1a). Individual Pt NPs exhibited a relatively large size

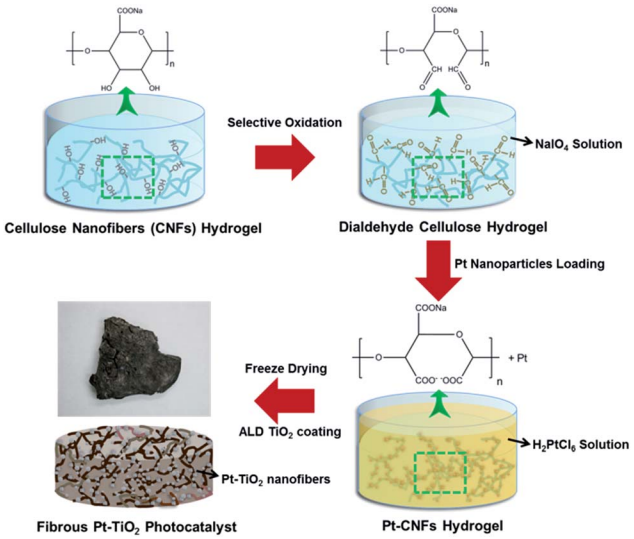

Scheme 1 Schematic representation of the preparation processes. The cellulose nanofiber (CNF) hydrogel is placed into $NaIO_4$ solution, which leads to the oxidation of hydroxyls to obtain a dialdehyde cellulose hydrogel. The hydrogel is thereafter transferred into H_2PtCl_6 solution for the growth of Pt nanoparticles. The cellulose hydrogel with Pt nanoparticles on the surface is finally treated by the freeze-dry method and the subsequent ALD TiO_2 thin film overcoating to achieve the nanofibrous Pt–TiO_2 photocatalyst.

distribution ranging from 20 nm to 80 nm (inset of Fig. 1a). Since the Pt NPs were produced by the aldehyde groups, changing the selective oxidation time would introduce different amounts of aldehyde groups to CNF surfaces and subsequently control the loading of Pt NPs. Three processing times, 144, 180, and 200 hours, were selected to oxidize the CNF templates, which were then used to produce Pt NPs within the same time frame and marked as C1, C2, and C3, respectively. CNF templates with a longer oxidation time yielded smaller Pt NPs, where the average NP sizes of C1, C2, and C3 were 80 ± 30, 40 ± 25, and 30 ± 10 nm, respectively (Fig. S5a–c†). The size reduction could be attributed to the increased number of surface functionalized aldehyde groups at a longer oxidation time, which induced a higher Pt nucleation rate in the beginning.[27,28]

The Pt NP-decorated CNF networks were then subjected to 300 °C ALD coating of a polycrystalline TiO_2 thin film (Fig. 1b and S5d–f†). While the highly porous CNF network structure was well preserved after ALD coating, most big Pt NPs were disappeared leaving mostly isolated tiny Pt NPs with an average size of 10 ± 3 nm (white spots in the inset of Fig. 1b and S5d–f†). Such a fusion phenomenon is common for metal NPs at elevated temperature due to the high surface energy and reduced melting point of small sized NPs. The high-temperature ALD process also decomposed the CNF template and left a pure TiO_2 tubular fiber network. The dark color of the as-prepared Pt–TiO_2 fibrous network has been identified as a result of the residual carbon elements in TiO_2 left by cellulose template pyrolysis.[24]

Elemental analysis of Pt decoration and TiO_2 ALD deposition was then conducted by X-ray photoelectron spectroscopy (XPS). As shown in Fig. 1c, the black and red curves illustrate the XPS

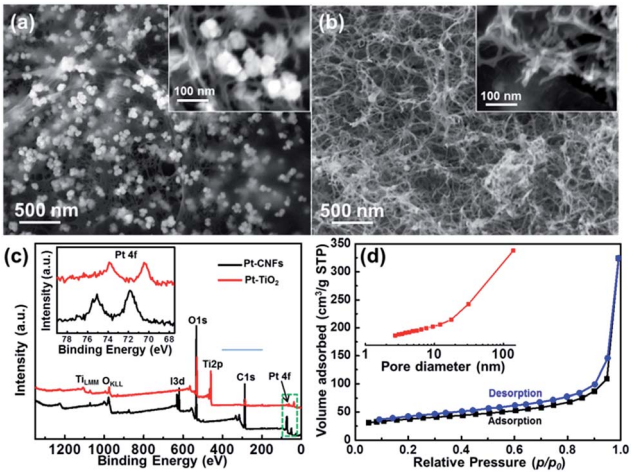

Fig. 1 Morphology and structure of Pt-CNF and Pt–TiO_2 samples. (a) Low magnification SEM images of nanofibrous Pt-CNFs; the inset shows the as-prepared free standing Pt-CNFs in a larger scale and the agglomeration of ~40 nm nanospheres on the nanostructured cellulose fibers. (b) Obtained fibrous Pt–TiO_2 network after ALD TiO_2 thin film overcoating at 300 °C; the inset reveals the Pt nanospheres on fibrous TiO_2. (c) X-ray photoelectron spectroscopy (XPS) investigation of both Pt-CNF and Pt–TiO_2 samples (black and red); the inset is the spectra of the Pt 4f region near ~71 eV. (d) Nitrogen adsorption–desorption isotherms and the corresponding pore-size distribution curves (inset) of the 3D fibrous Pt–TiO_2 composite.

profiles of Pt NP-decorated CNFs (Pt-CNFs) and structures after TiO_2 ALD coating (Pt–TiO_2). The peaks C 1s at 285.1 eV and I 3d at 619.9 eV in the Pt-CNF spectrum correspond to the carbon component and residual iodine of sodium periodate ($NaIO_4$)-treated cellulose. The drastically diminished C 1s peak and the disappearance of the I 3d peak in the Pt–TiO_2 sample suggested an effective removal of CNF templates leaving only residual carbon. This result was consistent with previous reports that calcination above 300 °C could completely decompose cellulose.[24,25,29] In addition, strong Ti related peaks (Ti 2p and TiLMM) appeared from the Pt–TiO_2 sample, supporting the fact that the CNFs were completely converted into Ti-based materials after ALD coating. The Pt 4f region near ~71 eV was further examined in detail to analyze the chemical structure of the Pt NPs before and after ALD processing (inset of Fig. 1c and S6a†). The Pt $4f_{7/2}$ and Pt $4f_{5/2}$ in Pt-CNFs are located at 71.8 eV and 75.2 eV, respectively. These two peaks shifted to 70.5 eV and 73.8 eV, respectively, after ALD of TiO_2 conversion. The higher 4f electron binding energy of the Pt-CNF structure can be attributed to the extra Pt–O bonds between Pt NPs and the carboxyl groups on CNFs.[30,31] The doublet lines in the Pt 4f spectrum of Pt–TiO_2 (70.5 eV and 73.8 eV) perfectly match the positions of metallic Pt.[32] The 3.3 eV difference between the binding energies of Pt $4f_{7/2}$ and Pt $4f_{5/2}$ peaks also indicates the presence of metallic Pt 4f states.[33] Moreover, compared to the Pt-CNF samples (C1, C2, and C3), the modified Auger parameters of Pt in the corresponding Pt–TiO_2 samples all shifted to the same position of metallic Pt[34,35] (green triangle) in the Wagner plot (Fig. S6b and S7†). Therefore, the relatively high temperature during ALD TiO_2 would be beneficial to the formation of pure metallic Pt, which is desirable for photocatalytic hydrogen generation.[15]

One intriguing advantage of the fibrous Pt–TiO_2 network structure is that it can provide a very high surface area. Therefore, Brunauer–Emmett–Teller (BET) surface area (S_{BET}) analysis was conducted to investigate this merit. Fig. 1d shows nitrogen adsorption–desorption isotherms and the associated Barrett–Joyner–Halenda (BJH) desorption pore size distribution curve (inset of Fig. 1d) obtained from the fibrous Pt–TiO_2 sample. A linear increase of the adsorption isotherm profile was observed in the relative pressure (p/p_0) range from 0.05 to 0.25, where the data were used to determine the S_{BET} of the Pt–TiO_2 sample using the multipoint BET method.[36] The obtained BET surface area was in the range of 128–166 $m^2\ g^{-1}$ (Table 1), which was much larger than the typical surface area of Pt–TiO_2 NP (~50 $m^2\ g^{-1}$) or nanowire (~30 $m^2\ g^{-1}$) arrays.[14,37,38] The hysteresis loop profile that appeared above the relative pressure (p/p_0) of 0.3 in the isotherm was classified as type IV according to the International Union of Pure and Applied Chemistry (IUPAC) categorization,[39] indicating the presence of mesopores. The rapidly increased adsorption at relative pressure close to unity ($p/p_0 = 1.0$) was similar to the isotherm of type II, revealing the coexistence of macropores.[39] In addition, desorption curve data were used to determine the pore size distribution by the BJH method, assuming a cylindrical pore model.[15,39] The pore size distribution (inset of Fig. 1d) shows that the fibrous Pt–TiO_2 network possessed a wide pore size distribution ranging from 3 to 140 nm, suggesting the co-existence of both mesopores and macropores. Such a porous structure would be particularly beneficial in photocatalysis, because it not only provides efficient mass pathways, but also offers an extremely large reaction interface between the catalyst and electrolyte.

Energy-dispersive X-ray spectroscopy (EDS) was performed on all three Pt-CNF template samples (C1, C2 and C3) and the

Table 1 Summary of the physical properties and photocatalytic activity of three 3D Pt–TiO_2 photocatalysts (T1, T2, and T3)

Pt–TiO_2 sample	Average Pt size (nm)	Pt wt%	S_{BET} ($m^2\ g^{-1}$)	H_2 production setup	Initial H_2 production rate (mmol $g^{-1}\ h^{-1}$)
T1	13	2.3	134.23	Capillary	100.56
				In electrolyte	25.88
T2	10	7.72	128.04	Capillary	138.69
				In electrolyte	62.11
T3	8	11.05	166.45	Capillary	128.30
				In electrolyte	44.82

corresponding Pt–TiO_2 samples (T1, T2 and T3). As shown in Fig. S8 and Table S2,† the Pt weight ratios of the C1, C2 and C3 samples were 20.2%, 33.26%, and 57.77%, respectively. A similar increasing tendency of Pt weight ratios was also observed for Pt–TiO_2 samples, suggesting that increasing the amount of aldehyde groups on CNFs could effectively raise the Pt NP loading to a substantially high level. The much lower Pt weight ratio would be a combined result of the replacement of CNFs by much heavier TiO_2 and the loss of a certain amount of Pt NPs due to the high temperature process. Additionally, inductively coupled-plasma (ICP) spectrometry was further performed on the three Pt–TiO_2 samples (T1, T2 and T3) to quantify the final Pt loading as a function of the oxidation time. The Pt emission peaks of the three samples at 265.945 nm showed intensity variations clearly (Fig. 2a). By referencing to standard Pt solution, the Pt weight ratios of the T1, T2 and T3 samples were 2.3%, 7.72%, and 11.05%, respectively (Fig. 2b). Such concentration values were similar to the values obtained by EDS (Fig. S8b†). Notably, the sodium and iodine signals coming from the functionalized CNFs in the EDS spectra were eliminated after the high temperature ALD TiO_2 overcoating, except the carbon signals. This suggested that most CNF templates were decomposed at 300 °C and some carbon elements were preserved in the final Pt–TiO_2 products, which has been found to be beneficial for possible visible light absorption and photoactivity in our previous work.[24]

Transmission electron microscopy (TEM) and X-ray diffraction (XRD) were implemented to study the crystal structure of the Pt NPs formed on CNF surfaces and the corresponding Pt–TiO_2 heterostructures. The low magnification TEM image clearly shows the network structure of CNFs with a fairly uniform thickness of ~15 nm, an average pore size of ~140 nm, and decorated with Pt NPs (Fig. 3a). The corresponding selective area electron diffraction (SAED) pattern (inset of Fig. 3a) exhibits the representative bright diffusive halo of cellulose[40] and diffraction spots of crystalline Pt. The crystalline structure of Pt NPs was further confirmed by XRD spectra, where the cellulose diffraction peak at 23° and the representative Pt (111) and (220) peaks were identified (Fig. S9 and S10†). An individual Pt NP rooted on the CNF surface is shown in Fig. 3b. The NP was ~80 nm in diameter and exhibited a spherical outline from the un-supported region. The relatively large contact area between the NP and CNF would be a result of the on-site reduction of Pt ions by the surface aldehyde groups. The spherical shape of the NP is indirect evidence of the nano-crystallinity of the Pt NP because no specific crystal facets could be observed in the NP. The high-resolution TEM (HRTEM) image (Fig. 3c) also revealed that the Pt NP was composed of numerous tiny crystallites. This observation suggested that the CNF surface aldehyde groups might produce a trace amount of Pt over the entire surface, which migrated and agglomerated into spherical Pt NPs in liquid media to minimize their surface energy.[41,42] The TEM

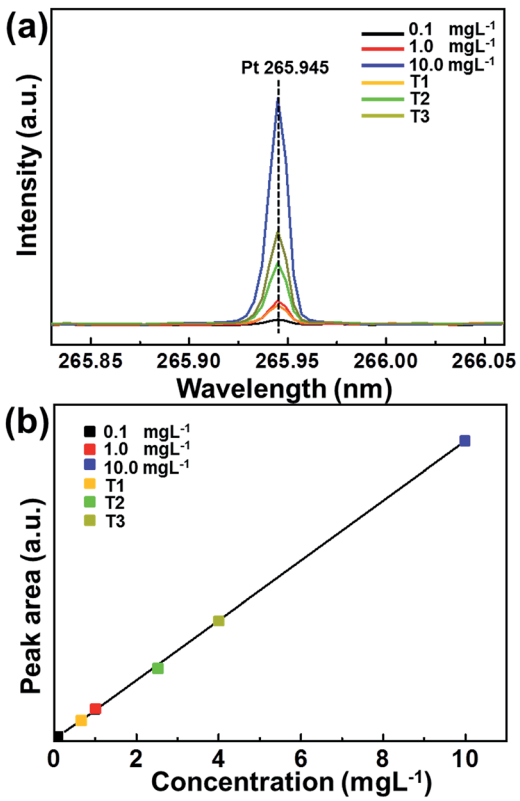

Fig. 2 Inductively coupled-plasma (ICP) spectrometry of three 3D nanofibrous Pt–TiO_2 samples prepared under different oxidation durations. (a) The Pt emission peaks of the three samples at 265.945 nm clearly show intensity variations compared to other three reference samples (0.1 mg L^{-1}, 1 mg L^{-1}, and 10 mg L^{-1}). (b) Corresponding emission peak areas *versus* Pt concentrations for three samples.

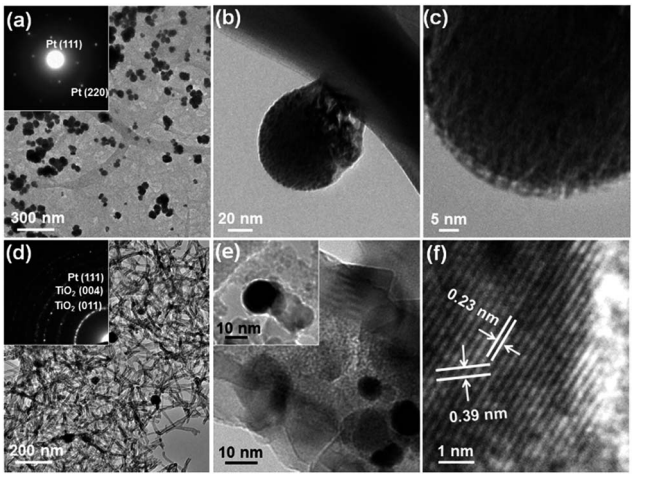

Fig. 3 Structures and the Pt nanoparticle distribution of samples before and after ALD TiO_2 coating. (a) TEM image of Pt-CNFs revealing a fibrous structure with Pt spheres on it; the inset is the respective SAD pattern. Only crystalline Pt appears on the Pt-CNFs before ALD TiO_2 coating. (b and c) Higher magnification images showing Pt nanospheres "rooted" on the surface of CNFs (b) and the Pt nanospheres aggregated from small nanoparticles (c). (d–f) TEM images of Pt–TiO_2 after ALD TiO_2 coating. (d and e) The fibrous TiO_2 with Pt nanoparticles indicating the well preserved morphology after the ALD process. (e) The ~17 nm thick polycrystalline TiO_2 is selectively deposited between Pt nanoparticles. (f) The measured lattice spaces of the nanoparticle are 0.39 and 0.23 nm, representing the corresponding values of Pt (100) and (111) planes.

image in Fig. 3d clearly shows the well-preserved fibrous structure after 170 cycles of ALD TiO_2 deposition at 300 °C, where more concentrated Pt NPs can also be observed. The SAED pattern further confirmed the anatase phase TiO_2 and crystalline Pt (inset of Fig. 3d). The thickness of the polycrystalline TiO_2 film was found to be ~17 nm (Fig. 3e), which was consistent with the typical morphology and growth rate of ALD TiO_2. Pt NPs were partially embedded in the TiO_2 film and the top portion was not covered by TiO_2 (inset of Fig. 3e). The exposure of the Pt NP was because $TiCl_4$ precursors would preferentially attach to the hydrophilic CNF surface that possesses abundant hydroxyl sites rather than to the inert Pt surface.[43,44] Meanwhile, the high temperature ALD process heat-treated the Pt NP simultaneously. This process was very helpful for improving the crystallinity of Pt NPs, removing chemical residues, and forming close contacts with TiO_2 crystals. Long-range-ordered Pt lattices can now be clearly observed by HRTEM. The lattice spacing of the Pt NP was measured to be 0.39 and 0.23 nm, corresponding to Pt (100) and (111) planes respectively. The anatase TiO_2 and crystalline Pt phases were also verified by the XRD spectra on all three Pt–TiO_2 samples (Fig. S10d†).

To fully demonstrate the advantage of cellulose templating, the out-of-electrolyte capillary design[24] was used to test the photocatalytic hydrogen generation behavior of the Pt NP decorated TiO_2 nanofiber network. The schematic setup is shown in Fig. 4a. The fibrous Pt–TiO_2 structure was attached to a piece of untreated CNF network. The bottom part of the CNF block was placed in a methanol solution to draw and transport the electrolyte to the Pt–TiO_2 photoactive surfaces. The testing apparatus for measuring the volumes of photocatalyzed gas evolution is shown in Fig. S1 and S2† (see the Experimental section for detailed measurement procedures). Upon illumination with a 70 W cm^{-2} Xe lamp source, H_2 rapidly evolved in air from the Pt–TiO_2 porous structure (no bubbles were formed in the electrolyte) and was collected in a quartz flask.

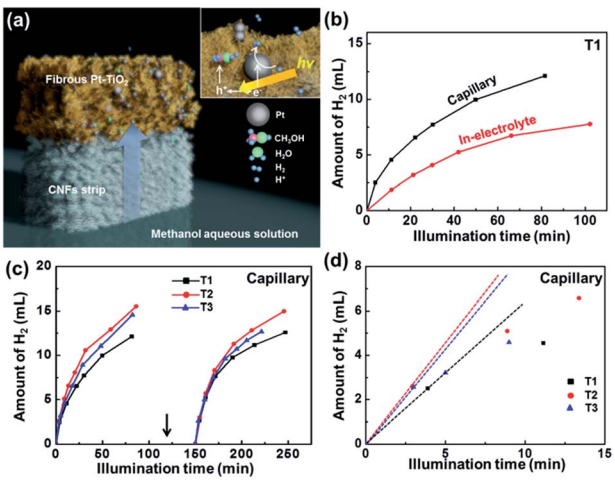

Fig. 4 (a) Schematics of the novel capillary design by using the CNF block for photocatalytic H_2 evolution. (b) H_2 yield of 3D nanofibrous Pt–TiO_2 sample T1 from both capillary design (black) and in-electrolyte design (red). (c) H_2 yield of three Pt–TiO_2 photocatalyst samples (T1, T2, and T3) *versus* illumination time in the capillary design. The curve after the electrolyte renewal and whole system purging indicates a good stability of the capillary setup for photocatalytic reactions. (d) Magnified H_2 evolution curves of the first 15 min in the presence of T1, T2 and T3 photocatalysts. Derived initial H_2 production rates were calculated by the indicated dashed lines.

The photocatalytic reaction mechanism of hydrogen production on the Pt–TiO_2 photocatalyst in methanol aqueous solution has been discussed in previous work.[14] As illustrated in the inset of Fig. 4a and S11,† the methanol adsorbs on the TiO_2 surface to form CH_3O–, which is able to capture the photogenerated holes for CH_3O. These methanol-derived groups can then be oxidized to form CH_2O, carbonate, or CO_2 eventually.[14] Meanwhile, the protons (H^+) were released during such a process. On the other hand, the photogenerated electrons can be trapped by Pt and thereafter react with H^+ for hydrogen generation.

In particular, in this capillary photocatalytic hydrogen generation process, the electrolyte was continuously supplied through the CNF network taking advantage of its excellent hydrophilic properties, and filled the mesopores within the Pt–TiO_2 network. When photoexcited electron–hole pairs were generated, they quickly dissociated at the Pt/TiO_2 interface with the electrons moving to the Pt NPs to reduce water generating H_2 and holes moving to the TiO_2 nanofibers to oxidize the electrolyte. Similar to the capillary PEC photoanode, enhanced photocatalytic reaction kinetics could be expected from the dynamic electrolyte supply and infinitesimal active electrolyte volume.[24]

The amount of generated H_2 was quantified for both capillary and conventional in-electrolyte setups using a Residual Gas Analyzer (RGA) (see details in the ESI†). Under the illumination of a 70 W cm^{-2} Xe lamp source, the capillary setup of 0.0157 g Pt–TiO_2 photocatalyst (sample T1) exhibited significantly higher H_2 yields compared to the in-electrolyte setup; while the H_2 production from both setups monotonically increased as a function of time (Fig. 4b). Initially, 4.6 mL H_2 was produced after 10 minutes of illumination from the capillary setup (black curve), which was three times higher than that from the in-electrolyte setup (red curve). With elongated reaction time, the H_2 generation rates decreased gradually and demonstrated a tendency of saturation after ~100 minutes of continuous reaction. The attenuation in H_2 production was more significant in the capillary setup, and thus the ratio between the yields of the two setups reduced from ~3.07 (at 10 minutes) to ~1.68 (at 80 minutes). Similar remarkable photocatalytic performance gain by the capillary setup, and the H_2 production attenuation phenomenon were both observed in Pt–TiO_2 samples T2 and T3 that had higher Pt loading (Fig. S12a and b†). To further investigate the reason of H_2 production attenuation, the reaction system was reset after 120 minutes of photocatalytic reaction. The resetting process included blocking of illumination, replacing methanol solution, and 30 minutes of system purging with argon (Ar) gas. After resetting the system, the initial H_2 generation recovered to its original rate for all three Pt–TiO_2 samples, while the same attenuation phenomenon was again observed for the extended photocatalytic reaction time (Fig. 4c). Furthermore, the Pt–TiO_2 photocatalysts were stored in

a regular lab environment for one month and then used to test their H_2 production ability again. As shown in Fig. S13,† the almost same tendency of the H_2 production was observed, which confirmed the good stability of this heterostructured capillary catalyst system. These results revealed that the catalytic performance of the Pt–TiO_2 structure was not impacted by the long-term operation and the attenuation of the H_2 production rate would be a result of kinetic factors. This kind of reaction rate drop was often observed in high-rate H_2 generation and other electrochemical processes,[16,19,45,46] particularly when the redox reactions occurred within very close vicinity.[47,48] Therefore, the non-linearity of H_2 yield *versus* time could be attributed to the reduced concentration of methanol solution and the accumulation of adsorbed product molecules (*e.g.* CH_2O and probably trace of H_2) that impede the accessibility of reactants.

Considering the kinetic factors that majorly influenced the long-term H_2 production, the initial H_2 generation rate was analyzed to understand the intrinsic photocatalytic properties. Fig. 4d shows the amount of H_2 collected at several time intervals within the first 15 minutes of illumination, from which the initial H_2 generation rate was obtained from the slope of the dashed line that connects the origin and first collected data point.[2,16] The same process was also applied to analyze the H_2 data of the in-electrolyte setup (Fig. S14†). All the data are summarized in Table 1. In general, the initial H_2 generation rates of capillary setups were significantly higher than those obtained from the in-electrolyte setup owing to less electrolyte related light scattering and better local reaction kinetics that we discovered in a previous study.[24] Specifically, the capillary setup exhibited an initial H_2 generation rate of 100.56 mmol g^{-1} h^{-1} from the Pt–TiO_2 photocatalyst T1; whereas the in-electrolyte setup from the same photocatalyst had only 25.88 mmol g^{-1} h^{-1}. The improvement by using the capillary setup reached 288.6%. The highest initial H_2 generation rate (138.69 mmol g^{-1} h^{-1}) was found from photocatalyst T2 that had higher Pt NP loading. However, the corresponding enhancement from the capillary setup was reduced to 123%. When the Pt loading was further increased to 11.05% (sample T3), the initial H_2 generation rates of both setups decreased to 128.30 mmol g^{-1} h^{-1} and 44.82 mmol g^{-1} h^{-1}, respectively, where the enhancement ratio jumped back to 186%. Due to the intrinsic photoabsorption limitation of TiO_2, these rate values were still lower than those of other advanced photocatalytic materials, such as $ZnIn_{0.25}Cu_xS_{1.375+x}$ and Pt–graphene–C_3N_4,[49,50] whereas enhanced performance from these materials could be expected by implementing the capillary PEC design.

The parabolic relationship between H_2 yield and Pt wt% (Fig. S15†) is in accordance with other published studies on metal catalyst loading.[14,19,51] While the absolute H_2 yield would further rise when the Pt NP loading was increased, the difference between the capillary and in-electrolyte setups reduced. The less sensitive H_2 generation rate to Pt loading of the capillary setup indicates that the capillary setup is more kinetically favorable and room for improvement is more limited compared to the conventional in-electrolyte configuration.[48] The overall significantly higher performance of the capillary photocatalytic design (Table 1) clearly shows that this setup can further enhance the H_2 evolution in addition to those achieved by other strategies, such as optimization of the Pt–TiO_2 surface area and Pt-loading amount. Given other key kinetic factors being well-engineered, the maximum H_2 evolution efficiency could be improved by implementing the capillary photocatalytic design.

Conclusions

In summary, aldehyde-functionalization of CNFs is an effective strategy to introduce Pt NPs onto CNF surfaces by on-site Pt ion reduction. A high concentration of Pt NP loading was achieved on $NaIO_4$-treated CNFs surfaces *via* on-site aldehyde reduction. Owing to the drastically different hydro-affinity of the Pt and CNF surfaces, ALD could selectively deposit TiO_2 on CNFs and kept the Pt NPs uncovered. The high temperature ALD process also simultaneously improved the crystallinity of Pt NPs and decomposed the CNF template leaving a pure anatase phase TiO_2 nanofiber network decorated with high-density Pt NPs (up to 11.05 wt%). The fibrous Pt–TiO_2 network photocatalyst was integrated with CNF strips to develop the capillary setup for photocatalyzed hydrogen generation. Owing to the excellent hydrophilic properties of CNFs, capillary force quickly and continuously supplied methanol electrolyte solution to the Pt–TiO_2 catalytic sites that were placed outside of the solution. Better reaction kinetics and higher efficiency were achieved from the capillary design compared to the conventional in-electrolyte reaction. The initial H_2 generation rates were found to be 100.56–138.69 mmol g^{-1} h^{-1} for the capillary setup based on different Pt NP loadings, which were 123.3–288.6% larger than those of the conventional in-electrolyte setup (25.88–62.11 mmol g^{-1} h^{-1}). The cellulose-based nanomanufacturing technique holds great promise for large-area, low-cost, and green fabrication of functional nanomaterials. The capillary photocatalytic design mimics the mass transport process in natural photosynthesis, where the interaction between light and reaction sites is no longer limited by the volume, surface and depth of the electrolyte. Therefore, this 3D nanofibrous Pt–TiO_2 photocatalyst offers a brand new solution for improving the throughput of photocatalytic hydrogen production.

Acknowledgements

This work is primarily supported by the U.S. Department of Energy (DOE), Office of Science, Basic Energy Sciences (BES), under Award # DE-SC0008711. CY thanks the support from the Forest Products Laboratory under Award # 14-JV-11111124-029 for CNF-related fabrication.

Notes and references

1 K. Ono, *Electr. Eng Jpn*, 2015, **190**, 1–9.
2 B. Rausch, M. D. Symes, G. Chisholm and L. Cronin, *Science*, 2014, **345**, 1326–1330.
3 X. Chen, S. Shen, L. Guo and S. S. Mao, *Chem. Rev.*, 2010, **110**, 6503–6570.

4 A. Fujishima and K. Honda, *Nature*, 1972, **238**, 37–38.
5 X. Wang, Z. Li, J. Shi and Y. Yu, *Chem. Rev.*, 2014, **114**, 9346–9384.
6 H. Kato, K. Asakura and A. Kudo, *J. Am. Chem. Soc.*, 2003, **125**, 3082–3089.
7 S. S. Mao and X. Chen, *Int. J. Energy Res.*, 2007, **31**, 619–636.
8 D. Duonghong, E. Borgarello and M. Graetzel, *J. Am. Chem. Soc.*, 1981, **103**, 4685–4690.
9 A. V. Vorontsov, E. N. Savinov and J. Zhensheng, *J. Photochem. Photobiol., A*, 1999, **125**, 113–117.
10 M. R. Hoffmann, S. T. Martin, W. Choi and D. W. Bahnemann, *Chem. Rev.*, 1995, **95**, 69–96.
11 S.-C. Moon, H. Mametsuka, S. Tabata and E. Suzuki, *Catal. Today*, 2000, **58**, 125–132.
12 R. Abe, K. Sayama and H. Arakawa, *Chem. Phys. Lett.*, 2003, **371**, 360–364.
13 A. Galińska and J. Walendziewski, *Energy Fuels*, 2005, **19**, 1143–1147.
14 T. Chen, Z. Feng, G. Wu, J. Shi, G. Ma, P. Ying and C. Li, *J. Phys. Chem. C*, 2007, **111**, 8005–8014.
15 J. Yu, L. Qi and M. Jaroniec, *J. Phys. Chem. C*, 2010, **114**, 13118–13125.
16 S. Tabata, H. Nishida, Y. Masaki and K. Tabata, *Catal. Lett.*, 1995, **34**, 245–249.
17 J. M. Herrmann, J. Disdier and P. Pichat, *J. Phys. Chem.*, 1986, **90**, 6028–6034.
18 C. Wang, L. Yin, L. Zhang, N. Liu, N. Lun and Y. Qi, *ACS Appl. Mater. Interfaces*, 2010, **2**, 3373–3377.
19 K. Sayama and H. Arakawa, *J. Chem. Soc., Faraday Trans.*, 1997, **93**, 1647–1654.
20 F. Zhang, J. Chen, X. Zhang, W. Gao, R. Jin, N. Guan and Y. Li, The ACS journal of surfaces and colloids, *Langmuir*, 2004, **20**, 9329–9334.
21 W. T. Yao, S. H. Yu, S. J. Liu, J. P. Chen, X. M. Liu and F. Q. Li, *J. Phys. Chem. B*, 2006, **110**, 11704–11710.
22 Y. Zheng, C. Chen, Y. Zhan, X. Lin, Q. Zheng, K. Wei and J. Zhu, *J. Phys. Chem. C*, 2008, **112**, 10773–10777.
23 H. Zeng, P. Liu, W. Cai, S. Yang and X. Xu, *J. Phys. Chem. C*, 2008, **112**, 19620–19624.
24 Z. Li, C. Yao, Y. Yu, Z. Cai and X. Wang, *Adv. Mater.*, 2014, **26**, 2262–2267, 2110.
25 Z. Li, C. Yao, F. Wang, Z. Cai and X. Wang, *Nanotechnology*, 2014, **25**, 504005.
26 X.-J. Huang, P.-C. Chen, F. Huang, Y. Ou, M.-R. Chen and Z.-K. Xu, *J. Mol. Catal. B: Enzym.*, 2011, **70**, 95–100.
27 J. K. Young, N. A. Lewinski, R. J. Langsner, L. C. Kennedy, A. Satyanarayan, V. Nammalvar, A. Y. Lin and R. A. Drezek, *Nanoscale Res. Lett.*, 2011, **6**, 428.
28 S. P. Shields, V. N. Richards and W. E. Buhro, *Chem. Mater.*, 2010, **22**, 3212–3225.
29 J. T. Korhonen, P. Hiekkataipale, J. Malm, M. Karppinen, O. Ikkala and R. H. Ras, *ACS Nano*, 2011, **5**, 1967–1974.
30 P. L. Antonucci, V. Alderucci, N. Giordano, D. L. Cocke and H. Kim, *J. Appl. Electrochem.*, 1994, **24**, 58–65.
31 R. Chebbi, A. Beicha, W. R. W. Daud and R. Zaamouche, *Appl. Surf. Sci.*, 2009, **255**, 6367–6371.
32 L. Qi, B. Cheng, W. Ho, G. Liu and J. Yu, *ChemNanoMat*, 2015, **1**, 58–67.
33 R. Yu, L. Chen, Q. Liu, J. Lin, K.-L. Tan, S. C. Ng, H. S. O. Chan, G.-Q. Xu and T. S. A. Hor, *Chem. Mater.*, 1998, **10**, 718–722.
34 C. J. Powell, *J. Electron Spectrosc. Relat. Phenom.*, 2012, **185**, 1–3.
35 C. J. Powell, *J. Electron Spectrosc. Relat. Phenom.*, 2010, **182**, 11–18.
36 S. Brunauer, P. H. Emmett and E. Teller, *J. Am. Chem. Soc.*, 1938, **60**, 309–319.
37 C. H. Lin, C. H. Lee, J. H. Chao, C. Y. Kuo, Y. C. Cheng, W. N. Huang, H. W. Chang, Y. M. Huang and M. K. Shih, *Catal. Lett.*, 2004, **98**, 61–66.
38 H. Chen, Z. Rui and H. Ji, *Ind. Eng. Chem. Res.*, 2014, **53**, 7629–7636.
39 K. S. W. Sing, *Pure Appl. Chem.*, 1985, **57**, 603–619.
40 H. Koga, E. Tokunaga, M. Hidaka, Y. Umemura, T. Saito, A. Isogai and T. Kitaoka, *Chem. Commun.*, 2010, **46**, 8567–8569.
41 J. Subero, Z. Ning, M. Ghadiri and C. Thornton, *Powder Technol.*, 1999, **105**, 66–73.
42 R. C. Cammarata, *Mater. Sci. Eng., A*, 1997, **237**, 180–184.
43 Q. Tao, G. Jursich and C. Takoudis, *Appl. Phys. Lett.*, 2010, **96**, 192105.
44 K. Overhage, Q. Tao, G. Jursich and C. G. Takoudis, *J. Undergrad. Chem. Res.*, 2011, **4**, 29–32.
45 W. Sheng, H. A. Gasteiger and Y. Shao-Horn, *J. Electrochem. Soc.*, 2010, **157**, B1529.
46 J. M. Nugent, K. S. V. Santhanam, A. Rubio and P. M. Ajayan, *Nano Lett.*, 2001, **1**, 87–91.
47 P. K. Adanuvor, *J.Electrochem. Soc.*, 1987, **134**, 625.
48 A. J. Bard and L. R. Faulkner, *Electrochemical Methods: Fundamentals and Applications*, Wiley, 2000.
49 Y. Li, G. Chen, Q. Wang, X. Wang, A. Zhou and Z. Shen, *Adv. Funct. Mater.*, 2010, **20**, 3390–3398.
50 X. Li, W. Bi, L. Zhang, S. Tao, W. Chu, Q. Zhang, Y. Luo, C. Wu and Y. Xie, *Adv. Mater.*, 2016, **28**, 2427–2431.
51 B.-S. Huang, F.-Y. Chang and M.-Y. Wey, *Int. J. Hydrogen Energy*, 2010, **35**, 7699–7705.